Alterable tension-compression asymmetry in work hardening of an additively manufactured dual-phase high-entropy alloy

Yunjian Bai [a,c], Kun Zhang [a,c,*], Tianyu Chen [a,c], Zishang Liu [a,c], Yunjiang Wang [b,c], Bingchen Wei [a,c,*]

[a] *Key Laboratory of Microgravity (National Microgravity Laboratory), Institute of Mechanics, Chinese Academy of Sciences, Beijing 100190, China*
[b] *State Key Laboratory of Nonlinear Mechanics, Institute of Mechanics, Chinese Academy of Sciences, Beijing 100190, China*
[c] *School of Engineering Science, University of Chinese Academy of Sciences, Beijing 100049, China*

ARTICLE INFO

ABSTRACT

High-entropy alloys (HEAs) as potential structural materials appear to exhibit tension-compression asymmetry (TCA) in work hardening. However, the intricate origin of the TCA, particularly in multi-domain HEAs, remains unclear. Herein, an additive manufactured AlCoCr-FeNi$_{2.1}$ dual-phase (FCC + BCC) HEA was used as a prototypical model system to gain a fundamental understanding of the TCA in multi-domain HEAs. Microscopic characterizations demonstrate that the TCA in work hardening is primarily attributed to the dominant stacking fault (SF)-dislocation interaction, SF-SF interaction, and subordinate twin-dislocation interaction, all of which are observed only in compression in the FCC phase. The former two mechanisms not only offer strong strengthening by impeding dislocation motion, but also bring considerable plasticity. The latter mechanism occurs in the dense SF regions to accommodate the plastic deformation, and contribute to additional work hardening. However, in tension, there are only dislocations generated inside the FCC phase. The marked difference in the deformation of the FCC phase is closely related to the FCC/BCC alternating lamellar heterostructure. Dislocations will preferentially nucleate and accumulate at the phase boundary, resulting in localized stress concentration. In tension, the stress concentration will lead to rapid crack propagation parallel to the phase boundary, resulting in premature failure of the sample. In compression, various types of cracks are formed and develop slowly, postponing the failure of the sample. Also, this TCA has the potential to be tuned by tailoring the FCC/BCC lamellar heterostructure; specifically, the width ratio of the FCC phase to the BCC phase. Our findings deliver cutting-edge insights relative to the TCA in new forms of alloys and offer a promising strategy to achieve the tunable possibility of the TCA in the work hardening by designing hierarchical heterostructures.

Introduction

The pursuit of metals or alloys with excellent mechanical properties has long been a focus in engineering (Sathiyamoorthi and Kim, 2022). However, a challenging problem is the difficulty of excavating new ones in conventional metallic materials. The advent of

high-entropy alloys (HEAs) enables the acquisition of new structural material candidates (Miracle and Senkov, 2017; Ye et al., 2016). Based on their superior mechanical properties such as ultrahigh yield strength of gigapascal (He et al., 2021; Zhang et al., 2021), excellent specific strength/stiffness (Gorsse et al., 2017; Nutor et al., 2021), a beneficial strength/ductility relationship (Cao et al., 2021; Liu et al., 2022), good fatigue resistance (Wang et al., 2020), and cold temperature fracture toughness (Gludovatz et al., 2014), HEAs are expected to be attractive structural materials in the future.

Despite their potential as excellent structural components, HEAs appear to exhibit anisotropy after yielding concerning to different deformation paths, i.e., the tension-compression asymmetry (TCA) in work hardening (An et al., 2020; Joseph et al., 2017). This may be some different from the conventional alloys that show a conspicuous TCA in yielding. In general, the TCA in yielding of the conventional alloys (e.g., Mg alloys (Habib et al., 2017; Yin et al., 2021), Inconel alloy (Ghorbanpour et al., 2020), Al-Fe alloys (Li et al., 2020)) is often attributed to the sensitivity differences of defects to deformation paths due to texture and/or crystal orientation, which has been widely confirmed by electron microscopic experiments and atomic simulations. A. S. Khan, W. Liu and the relevant co-operators (Habib et al., 2017; Khan et al., 2012; Khan and Liu, 2012; Khan and Yu, 2012; Ku et al., 2020) deeply studied the TCA phenomenon in different alloys through finite element simulation, and proposed a series of criterions or methods for describing anisotropic yielding, which greatly enriches our understanding of the TCA in yielding of the conventional alloys. However, the understanding of the TCA in work hardening of the HEAs remains greatly lacking, which may seriously limit the engineering applications of these HEA components. For instance, HEA components subjected to bending loading (e.g., beams, tubes, and plates) will simultaneously sustain tension and compression. The presence of TCA in the work hardening will lead to a large deformation mismatch between the tension section and compression section (Suryawanshi et al., 2021), resulting in one fracturing first in comparison to the other. To understand the full potential of HEAs as excellent structural materials, it is necessary to clarify the origin and achieve the tunability of TCA in the work hardening.

For single-domain HEAs, various mechanisms of TCA in the work hardening have been elucidated. For example, Joseph et al. (2017) first emphatically reported TCA in work hardening of the $Al_{0.3}CoCrFeNi$ HEA with a single face-centered cubic (FCC) solid solution. It was observed that the significant TCA in this alloy was attributed to the profuse mechanical twinning generated in compression but not in tension. An et al. (2020) also reported a similar trend of TCA in the $Fe_{40}Co_{20}Cr_{20}Mn_{10}Ni_{10}$ HEA with a single FCC solid solution. It was observed that the conspicuous TCA in this alloy is attributed to the martensite phase transformation from FCC to hexagonal closed packed (HCP) that predominantly occurs in compression (compared to tension). Their findings have important implications for understanding TCA in the work hardening of HEAs (especially the single-domain HEAs). However, for multi-domain HEAs, the origin of TCA in the work hardening may be complicated because the deformation behaviors of various domains are rather diverse during deformation (Bai et al., 2021; Fu et al., 2022; Hasan et al., 2019; He et al., 2021; Li et al., 2020; Ma and Wu, 2019; Nutor et al., 2021; Wu et al., 2019); in particular, Fang et al. (Fang et al., 2019) earlier investigated the effect of different phase volume fractions of a dual-phase HEA on mechanical properties using atomistic simulations, thereby verifying the heterogeneity of the different phases/domains during deformation on atomic-scale mechanism. Understanding how the different domains interact to influence TCA in the work hardening remains unclear. To the best knowledge of the authors, there has been no cutting-edge coverage of TCA in the work hardening of the multi-domain HEAs. Therefore, to clarify the origin of TCA in the work hardening of the multi-domain HEAs and realize its adjustability, it is critical to (i) uncover the deformation behaviors of various domains in different deformation pathways, and (ii) reveal the TCA response to different combinations (such as different fractions or sizes) between various domains.

In this work, to acquire in-depth insights into the origin of TCA in the work hardening of multi-domain HEAs, the $AlCoCrFeNi_{2.1}$ dual-phase HEA (DP-HEA) composed of FCC and body-centered cubic (BCC) phases has been fabricated by additive manufacturing. Three laser powers from high to low were used to prepare the DP-HEA with distinct microstructures, such as different phase widths and fractions of the FCC phase and BCC phase. During deformation, the respective responses of the FCC phase and BCC phase were systematically characterized and investigated by electron backscatter diffraction (EBSD) and transmission electron microscopy (TEM). The mechanism of the TCA in the work hardening of this DP-HEA was discussed, and the effects of different microstructural combinations on this TCA were investigated in detail. Finally, the possibility of designing hierarchical heterostructures to tune TCA in the work hardening of HEAs was proposed.

Materials and methods

2.1. Material preparation and mechanical testing

The DP-HEA was fabricated by an LMD-1500 printing machine (self-developed, Automation Research Institute Co., Ltd., China South Industries Group Corporation, Mianyang) that is a direct energy deposition pattern. The pre-alloyed powder was prepared via vacuum induction melting gas atomization. The powder size was controlled between 45 μm to 105 μm. The scanning speed was 600 mm/min, and the layer thickness was 250 μm. From high to low, the laser powers were selected as 1200 W, 900 W, and 600 W. Generally, the scanning strategy is unidirectional scanning. The deposited DP-HEA was then transferred from the 316-steel substrate using wire cutting. Before cutting, the DP-HEA and substrate were heat-treated at 650 °C for 3 h to remove accumulated thermal stresses, thereby preventing large deformation during wire cutting. Cylindrical specimens for compression were cut to Φ5 × 10 mm, and dog-bone specimens for tension were cut to 10 mm × 3 mm × 1.5 mm gage length. All specimens were ground and polished to remove surface defects before mechanical testing. Quasi-static tensile tests were performed on an MTS Landmark electro-hydraulic servo mechanics test system, and the quasi-static compressive tests were performed on an LD26 universal testing machine. Both the tensile and compressive tests were run at a steady strain rate of $1 \times 10^{-3} s^{-1}$ at room temperature. At least three times for samples in

each condition were tested to ensure repeatability.

2.2. Microstructural characterization

To investigate the microstructures of the printed DP-HEA before and after deformation, EBSD, TEM, and high-resolution TEM (HRTEM) were conducted. EBSD was carried out on a scanning electron microscope (SEM JSM-7100F) with OIM-analyzed software. Before observation, all EBSD specimens were vibration polished to acquire a good Kikuchi pattern. TEM and HRTEM observations were conducted on a JEOL JEM-2100F field emission instrument at 200 kV, to identify the deformation characteristics inside the samples after compression and tension. TEM specimens were cut out from the corresponding deformed samples and carefully ground into foils with a thickness of about 50 μm, and then prepared by twin-jet polishing systems. The electrolyte was made of 90 vol% alcohol and 10 vol% perchloric acids and operated at −25 °C (Gao et al., 2017).

Results

3.1. Microstructures of the DP-HEA modified by additive manufacturing

Fig. 1 illustrates the microstructures of the DP-HEA printed at various laser powers. It can be observed that all printed samples are composed of exclusively columnar grains with a regular eutectic lamellar structure with no obvious texture, as shown in Fig. 1(a)–1(c), the inverse pole figure (IPF) map. As the laser power gradually decreases, the columnar grain size gradually decreases, which, at a fixed magnification, shows that the DP-HEA printed at 600 W contains the most columnar grains. In addition to the columnar grain size, the phase width and fraction also exhibit visible dependence on laser power; see EBSD phase maps of Fig. 1(d)–1(f). Specifically, with laser
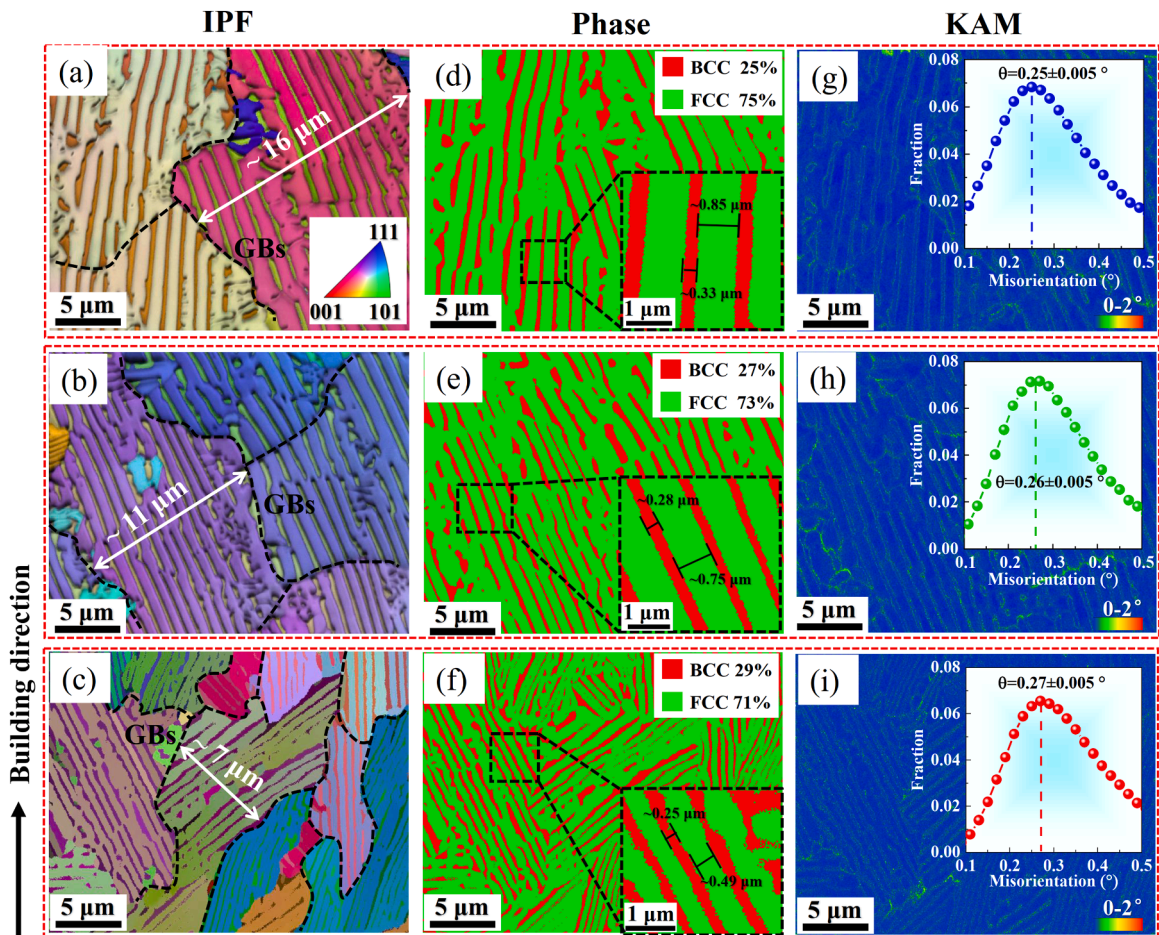

Fig. 1. Microstructures of the DP-HEA printed at various laser powers. IPF maps of the sample printed at (a) 1200 W, (b) 900 W, and (c) 600 W, showing grain size information. EBSD phase maps of the sample printed at (d) 1200 W, (e) 900 W, and (f) 600 W, depicting the fraction and width of the BCC phase and FCC phase. KAM maps of the sample printed at (g) 1200 W, (h) 900 W, and (i) 600 W, suggesting lattice distortion at the phase interface, where the insets are the corresponding quantized KAM values.

power gradually decreasing, the phase width of both the FCC phase and BCC phase decrease, whereas the BCC phase fraction gradually increases while the FCC phase fraction gradually decreases. The kernel average misorientation (KAM) maps indicate, except for the phase interface, the KAM value is almost zero due to the annealing treatment, as shown in Fig. 1(g)–1(i). This result demonstrates that lattice distortion exists at the phase interface, owing to the mismatch of atoms from the FCC phase into the BCC phase, and this is verified by the large misorientation of ~43° between the FCC phase and BCC phase in Fig. S1. Therefore, the more phase interfaces (i. e., the smaller the phase width), the larger the KAM value. Due to the highest fraction of the BCC phase, the sample printed at 600 W has more phase interfaces than the other two cases, leading to a high average KAM value (0.27±0.005°), which is larger than that of the samples printed at 1200 W (0.25±0.005°) and 900 W (0.26±0.005°).

As shown in Fig. 1, the laser power can significantly affect the microstructures of the DP-HEA created during additive manufacturing. The quantized information is provided in Fig. 2. As can be seen in Fig. 2(a), with the laser power decreasing from 1200 W to 600 W, the columnar grain size decreases from ~16 μm to ~7 μm. Next, the FCC phase width decreases from ~0.85 μm to ~0.49 μm, and the BCC phase width decreases from ~0.33 μm to ~0.25 μm, which are reductions of ~56% and ~24%, respectively. The difference in phase width between the FCC phase and BCC phase of the DP-HEA printed at 600 W is the smallest. Third, the width ratio and fraction ratio of the FCC phase to the BCC phase are also sensitive to the laser power, where the former first increases and then sharply decreases while the latter monotonously decreases (Fig. 2(b)). The DP-HEA printed at 600 W has the smallest width ratio of 1.96, which is far lower than that printed at 1200 W and 900 W, which are both greater than 2.5.

3.2. Mechanical performance of the DP-HEA

The mechanical properties of the DP-HEA printed at 1200 W, 900 W, and 600 W are provided in Fig. 3(a), and the results are summarized in Table 1. The printed samples exhibit excellent compressive behavior, with a good combination of both high strength and ductility. The yield strength is more than 900 MPa, the ultimate strength is more than 2000 MPa, and the uniform elongation is more than 28%. In particular, the DP-HEA printed at 600 W possesses the highest compressive yield strength (1041 MPa) due to the Hall-Petch effect. The tensile properties indicate that all samples have the similar strength, but a very different uniform elongation. The 600 W-printed sample possesses a maximum uniform elongation of 5.8%. Compared to the compressive behaviors, the ultimate tensile strength and uniform elongation are inferior, while the tensile yield strength is comparable. Therefore, the DP-HEA exhibits a negligible TCA in yielding but a noticeable TCA in work hardening. In addition, this TCA level of the DP-HEA printed at different laser powers shows conspicuous distinction. Direct evidence of this is the plasticity difference ($\Delta\varepsilon$) between compression and tension of the different samples. As shown in Table 1, the $\Delta\varepsilon$ values of the DP-HEA printed at 1200 W, 900 W, and 600 W are 0.260, 0.277, and 0.222, respectively. The $\Delta\varepsilon$ of the DP-HEA printed at 600 W is far less than those printed at 1200 W and 900 W, which indicates that the DP-HEA printed at 600 W exhibits relatively good symmetry between compression and tension compared to the other two levels of laser power, and may have the lowest magnitude of TCA in work hardening.

To comprehensively evaluate the TCA behavior of the DP-HEA, two dimensionless parameters are defined:

$$D_1 = \sigma_{CY} / \sigma_{TY} \qquad (1)$$

$$D_2 = \frac{\int (\sigma_c - \sigma_{CY})d\varepsilon_c, \ \sigma_c \geq \sigma_{CY}}{\int (\sigma_t - \sigma_{TY})d\varepsilon_t, \ \sigma_t \geq \sigma_{TY}} \qquad (2)$$

where σ_{CY} and σ_{TY} represent the compressive yield strength and tensile yield strength, respectively, σ_c and σ_t represent the compressive flow stress and tensile flow stress, and ε_c and ε_t represent the corresponding compressive flow strain and tensile flow strain, respectively. Eq. (1) represents the yield strength ratio, often reflecting the TCA in the yielding (Chen et al., 2021; Sun et al., 2019), and Eq.
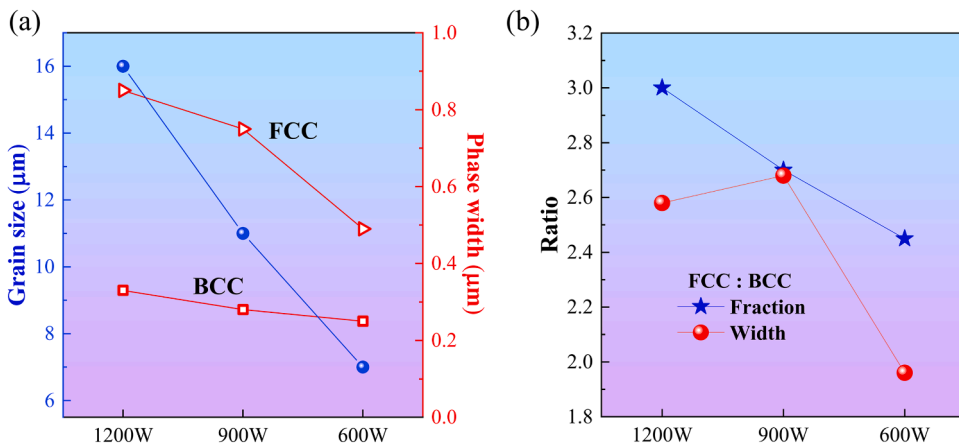

Fig. 2. (a) Grain size and phase width of the DP-HEA printed at various laser powers. (b) Width ratio and fraction ratio of the FCC phase to the BCC phase.
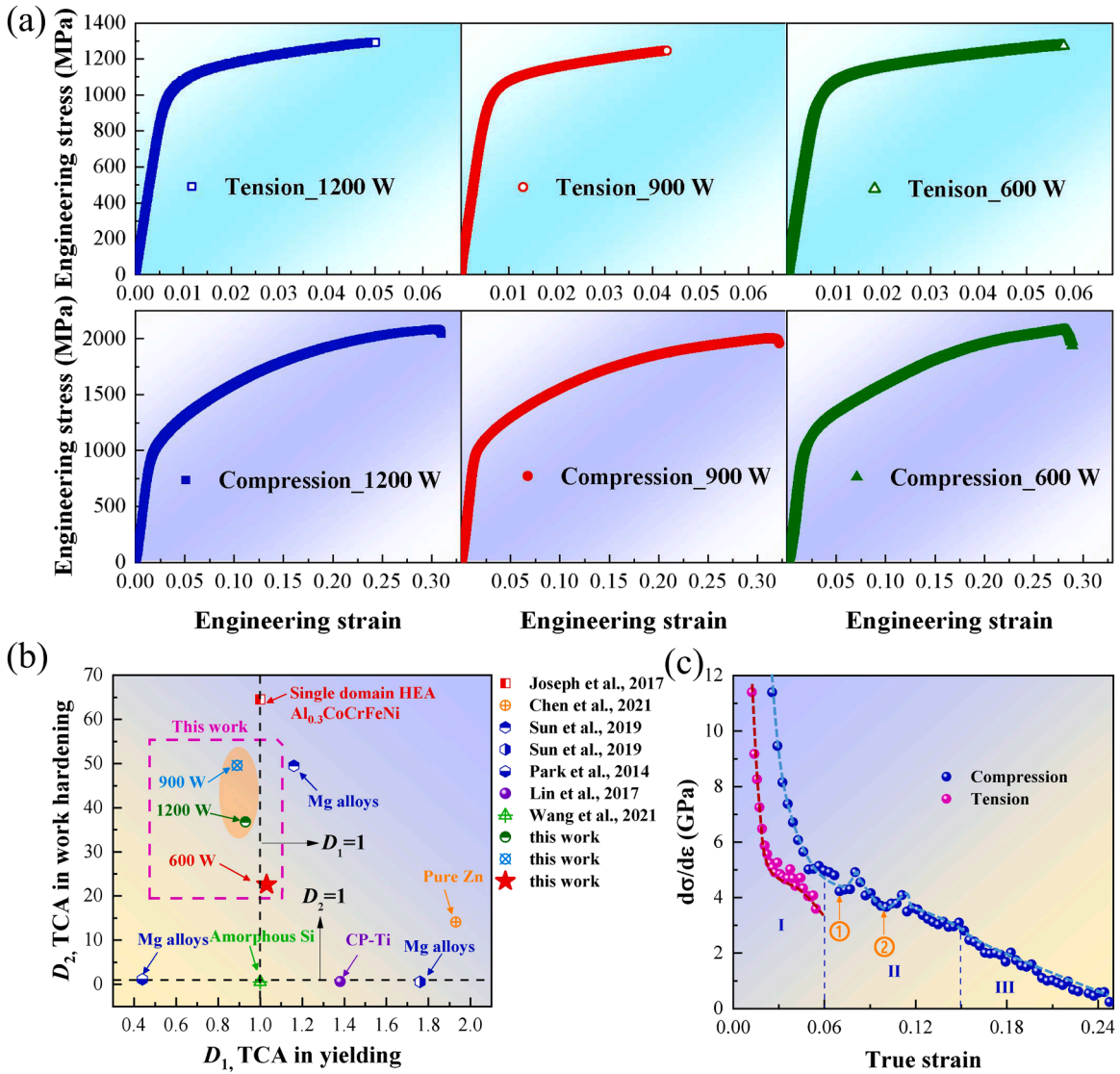
Fig. 3. (a) Tensile and compressive properties of the DP-HEA printed at various laser powers. (b) Relationship between D_1 and D_2, indicating that the 600 W-printed sample has a weaker TCA in work hardening. (c) The work hardening rate of the 600 W-printed sample.

Table 1
Mechanical properties of the DP-HEA printed at various laser power levels.

Sample	Yield Strength (MPa)		Ultimate strength (MPa)		Elongation (%)	
	Com.	Ten.	Com.	Ten.	Com.	Ten.
600 W	1041±28	1035±21	2072±52	1273±25	28±1.4	5.8 ± 0.29
900 W	966±37	1001±40	2003±46	1246±37	32±2.1	4.3 ± 0.13
1200 W	925±35	958±32	2084±61	1292±33	31±1.9	5.0 ± 0.31

(2) represents the ratio of the stress increment to the area enclosed by the strain after yielding, which can be used to reflect TCA in the work hardening. Fig. 3(b) depicts the relationship between D_1 and D_2. HEAs exhibit a converse tendency compared with conventional metals and alloys. For example, pure Zn (Chen et al., 2021), Mg alloys (Park et al., 2014; Sun et al., 2019), and CP-Ti (Lin et al., 2017) frequently have a noticeable TCA in the yielding, but after yielding, the work hardening is not significantly anisotropic in different deformation paths. However, HEAs often exhibit significant TCA in the work hardening but not in the yielding. This infers that the deformation mechanism of HEAs is very different between compression and tension after yielding. In addition, as shown in Fig. 3(b), all of the D_2 values of the DP-HEA samples are far lower than that of the single-phase $Al_{0.3}CoCrFeNi$ HEA, indicating that the DP-HEA

shows a reduced TCA in the work hardening than in single-domain HEAs. Moreover, the D_2 of the DP-HEA printed at 600 W is ~22, which is significantly lower than those printed at 1200 W and 900 W, and closer to ideal symmetry such as in amorphous Si (Wang et al., 2021). This indicates that the TCA in the work hardening of the DP-HEA is alterable by tailoring the lamellar heterostructure.

Fig. 3(c) depicts the work hardening rate of the DP-HEA printed at 600 W. At a glance, the work hardening rate curve during compression is complicated, and the entire process can be divided into three regimes. In regime I, the true strain is less than 0.06, and the work hardening rate drops sharply and monotonously with increasing strain. In regime II, the true strain is between 0.06 and 0.15, and the work hardening rate slowly decreases from 5 GPa to 3 GPa per strain. While the work hardening rate decreases with increasing strain overall, there are two 'strange' stages where the work hardening rate briefly increases with increasing strain, which are marked by yellow arrows in this regime. In regime III, the true strain exceeds 0.15, and the work hardening rate continues to decrease monotonously with increasing strain. The tensile work hardening rate curve is relatively simple, showing that the work hardening rate sharply decreases with increasing strain until fracture.

3.3. Deformation characteristics of the FCC/BCC phases

To reveal the deformation characteristics of the FCC phase and the BCC phase, the KAM value at different strain under tension and compression are illustrated in Fig. 4. Generally, KAM was used to reflect the defect concentration of the deformed samples, where the larger the KAM value, the more defects in the deformed samples (Bai et al., 2021; Calcagnotto et al., 2010; Qin et al., 2022). The KAM value of the FCC and BCC phases at the tensile strain of 0.058 (i.e., the fractured strain) are 0.37±0.04 ° and 0.29±0.05°. These values are similar to those corresponding values at the compressive strains of 0.055, respectively, 0.36±0.06° and 0.30±0.05°. This indicates that the early deformation modes in tension and compression are probably identical. In addition, the KAM value of the BCC phase is quite small under this relatively small strain, which is close to the value (~0.27°) before deformation. This suggests that the BCC phase hardly undergoes plastic deformation at the early stage either in tension or compression. With compressive strain increasing, the KAM values of both the FCC and BCC phases increase. However, the increase rate is significantly different. As can be seen in Fig. 4(c), the KAM value of the FCC phase increases significantly faster than that of the BCC phase, indicating that during deformation, the distribution of plastic deformation is increasingly dominated by the FCC phase due to the limited plastic deformation capacity of the BCC phase. The KAM value of the BCC phase hardly increases at the imposed strain from 0.15 to 0.25, which can be inferred that the plastic deformation of the BCC phase is close to the upper limit when the strain exceeds 0.15. However, the KAM value of the FCC phase continuously increases noticeably with the strain increasing. More interestingly, the KAM increment of the FCC phase is largest at the imposed strain from 0.10 to 0.15. This strain interval is inside regime II of the work hardening rate in Fig. 3(c), which demonstrates that in this strain interval, new deformation mode or mechanism may have occurred, thereby resulting in the 'strange' stages.

To further explain the defect distribution features within the FCC and BCC phases after fracture, GND density within the FCC and BCC phases of the fractured samples are depicted in Fig. 5. In compression, the FCC phase has a high and homogeneous GND density, whereas the BCC phase has a low GND density that is mainly distributed at the phase boundaries. In tension, the GND density within the FCC phase is uneven, showing a gradient distribution from the phase interface to the interior. In addition, there is almost no GND within the BCC phase, verifying that the plastic deformation is almost entirely provided by the FCC phase at the early deformation stage. Fig. 5(c) illustrates the specific KAM trend inside single FCC island and single BCC island. For comparison, the undeformed sample is measured as a baseline. The starting point and end point of the profiles are the phase interfaces on both sides, and the profile shows the KAM of an arbitrary point to the origin point. For the FCC phase, the compressive sample exhibits a uniform misorientation distribution with a larger value of ~1.5° compared to the baseline (~0.25°), implying homogeneous and severe plastic strain; however, the tensile sample shows an obvious gradient distribution of misorientation, with a strain gradient from the phase boundary to the interior. For the BCC phase, although the misorientation of the compressive sample exhibits the same tendency as that of the FCC
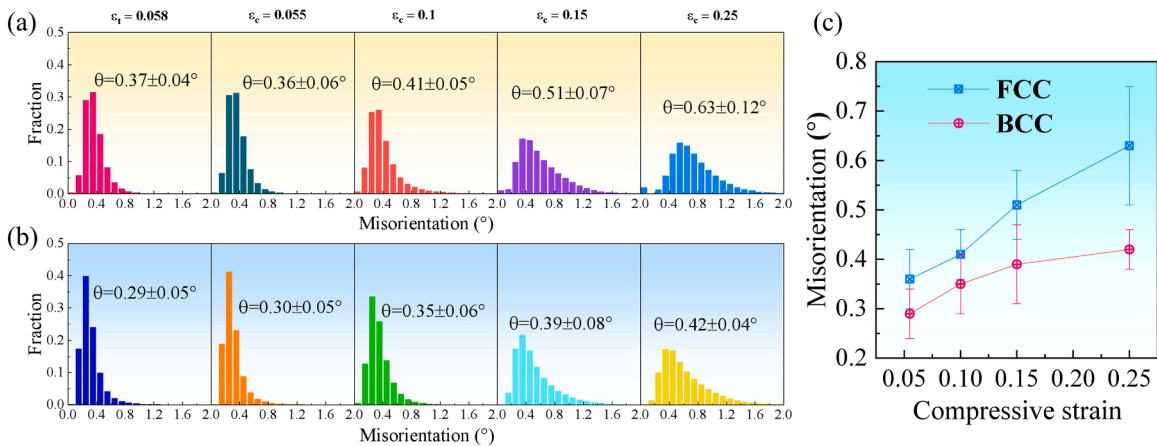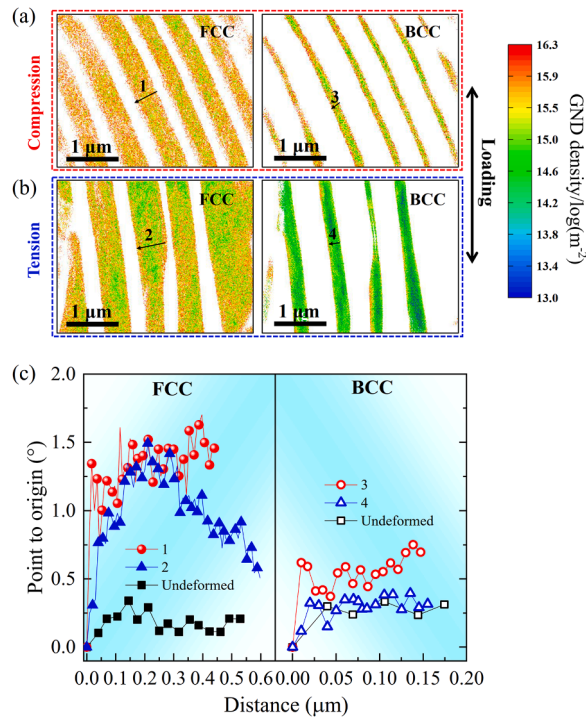

Fig. 4. The KAM value at different strain stages under tension and compression: (a) the FCC phase, (b) the BCC phase. (c) Variation trend of the KAM value of the FCC and BCC phases with compressive strain increasing.

Fig. 5. GND density heat maps of the fractured samples: (a) compression and (b) tension. (c) The KAM misorientation inside the FCC phase and BCC phase marked in (a) and (b), respectively.

phase, the value is only ~0.5°, indicating that the BCC phase contributes to minor plastic deformation; the tensile sample shows that the profile almost coincides with the baseline, inferring almost no plastic deformation of the BCC phase.

The results of Fig. 5 not only confirm the KAM results in Fig. 4, but also intuitively present the specific distribution of dislocations in the FCC and BCC phases. It is also found that although the compressive strain is much larger than the tensile strain, the GND density inside the BCC phase of the compressive fractured sample is still relatively low. Therefore, it is reasonable to speculate that the BCC phase may not behave strong differently between compression and tension.

Postmortem TEM observations of the DP-HEA are provided in Fig. 6. The deformation characteristics of the FCC phase and BCC phase are quite different in the deformed sample, especially in the compressive sample.

The compressive sample

Within the FCC phase, there is a high dislocation density (HDD) in the form of dense dislocation networks (Fig. 6(a)). In addition to the HDD, extensive stacking faults (SFs) marked by yellow arrows are also observed within the FCC phase. The SFs are multi-directional and form into the SFs intersection marked by the yellow dashed line in the inset of Fig. 6(b). The profuse SFs can be seen as a strong barrier to dislocation movement (Jian et al., 2013). As a result, a large number of dislocation tangles (DTs) marked by a blue dashed circle in Fig. 6(b) are gathered in dense SFs regions, owing to the multitude of SF-dislocation interactions. The multi-directional SFs are also supported by the HRTEM observation in Fig. 6(c). The SFs in different directions are formed into SFs intersection, which is further formed into an SFs loop marked by green dashed rhombus, indicating strong SF-SF interactions. The intensive SF-dislocation and SF-SF interactions generally result in strong strain hardening by impeding dislocation motion (Frank et al., 2020; Nutor et al., 2021; Xu et al., 2018), and thus, mechanical twins (MTs) may be preferentially generated under this condition to accommodate plastic deformation (Jeong et al., 2018). However, as seen in Fig. 6(a) and 6(b), MTs are not detected within the FCC phase at low magnification. Instead, MTs are observed at an HRTEM image of the dense SFs region; see Fig. 6(d) and its inset of the FFT pattern. The MTs are only nanoscale with a thickness of less than 5 nm and are surrounded by numerous SFs. This means that although twin-dislocation interactions can further bring additional hardening and contribute to plasticity, it is subordinate compared to the SF-dislocation and SF-SF interactions. This is very different from the dominant twinning-induced work hardening in low stacking fault energy (SFE) HEAs (Deng et al., 2015; Joseph et al., 2017), which may be attributed to the unique alternating lamellar heterostructure.

Within the BCC phase, however, only a relatively low dislocation density (LDD) in the form of dislocation lines marked by light cyan arrows in Fig. 6(a) are generated, and few DTs are formed at the phase boundary. These results demonstrate that the FCC phase deformed severely and homogeneously, which is attributed to the HDD and extensive SFs as well as nanoscale MTs, whereas the BCC phase is difficult to deform plastically and only yields LDD. Therefore, the DP-HEA exhibits severe heterogeneous deformation between the FCC phase and BCC phase in compression.

Compression
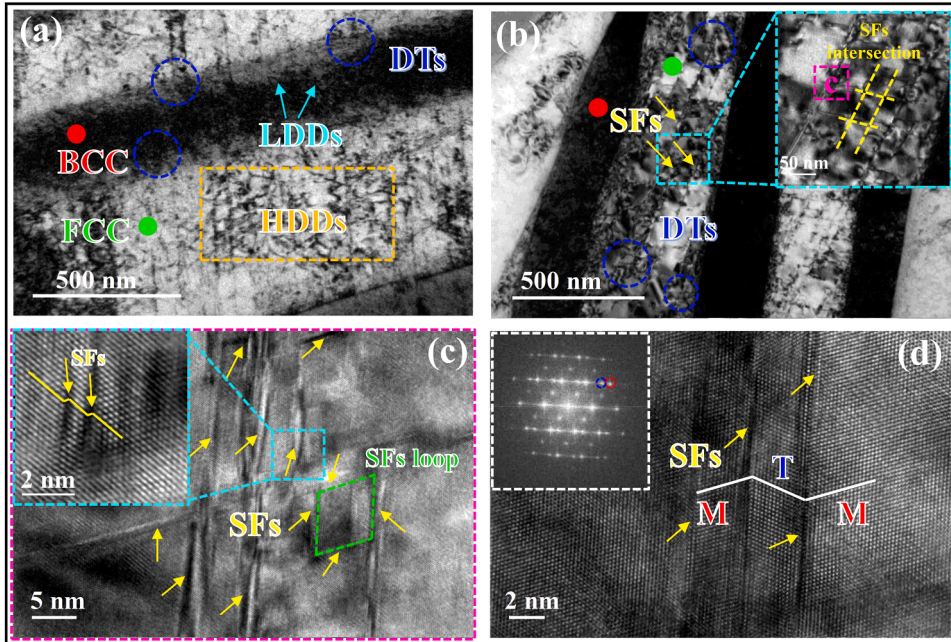
Tension
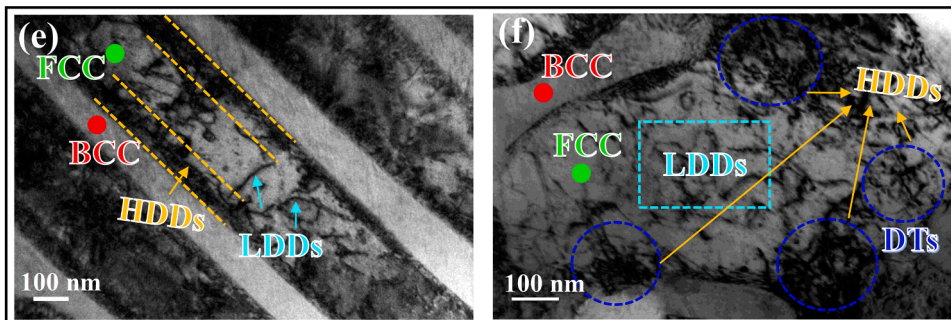
Fig. 6. Typical TEM bright-field images of the DP-HEA after fracture. After compressive fracture: (a) HDD within the FCC phase and LDD within the BCC phase. (b) Extensive multi-directional SFs within the FCC phase, where the inset indicates the formed SFs intersection. (c) HRTEM observation of the SFs intersection marked in the enlarged view of (b), showing the formation of the SFs loop. (d) HRTEM image of the nanoscale MTs, where the inset is the corresponding fast Fourier transform (FFT) pattern. After tensile fracture: (e) HDD at the phase boundary and LDD inside the interior of the FCC phase, with no visible dislocations within the BCC phase. (f) Dislocations inside the FCC phase accumulated at the phase boundary, forming a large number of DTs. All the TEM sectioning is done parallel to the loading axis.

The tensile sample

The deformation characteristics of the tensile sample are relatively simple. The dislocations within the FCC phase are inhomogeneous. As seen from Fig. 6(e), HDD are formed at the phase boundary but LDD are formed at the phase interior, showing an obvious gradient distribution from the phase boundaries to the interior, which is very consistent with the EBSD result in Fig. 5(b). In addition, a large number of dislocations are piled up at the phase boundary to form into numerous DTs marked by blue dashed line circles (Fig. 6 (f)). Dislocations accumulated at the phase boundary will result in severe localized stress concentration (Cepeda-Jiménez et al., 2019; Jiang et al., 2018), which may lead to premature breakage during tension. This is reasonable given that the tensile behavior of the DP-HEA showed inferior plasticity. In addition, except for dislocations, no visible SFs and MTs are identified within the FCC phase, and no visible dislocations are observed within the BCC phase. This indicates that almost all plastic deformation of the DP-HEA is provided by the dislocation slip inside the FCC phase during tension.

The TEM results are in good agreement with the EBSD results, i.e., the DP-HEA exhibits significant heterogeneous deformation between the FCC phase and BCC phase either in compression or tension. The heterogeneous deformation is more pronounced especially in compression because the FCC phase is not only much higher in dislocation density than the BCC phase, but also contains a large number of SFs as well as MTs.

4. Discussion

4.1. Deformation mechanisms in tension and compression

To interpret the TCA in the work hardening of the DP-HEA, the deformation mechanisms of compression and tension in the different regimes are discussed. Based on the result of Fig. 4, the deformation mode in regime I in compression can be deduced from the deformation characteristics of the tensile fracture sample, since their early deformation modes may be same.

Regime I (the whole process of tension): The FCC phase begins to deform plastically, while the BCC phase is still in an elastic stage. Dislocations originating inside the FCC phase (preferentially at/near the phase boundary) are continuously emitted towards the BCC phase, blocked by, and piled up at the phase boundary to form DTs eventually. Hence, there is a strain gradient inside the FCC phase from phase boundary to the interior (Fig. 6(e)), whereas no visible dislocations are observed within the BCC phase.

Regime II: With increasing strain, the BCC phase also begins to plastically deform to yield dislocations. Meanwhile, a large number of SFs are generated inside the FCC phase. The SFs, involving dissociations of dislocations (Jian et al., 2013), will hinder the movement of dislocations (DTs are formed in dense SFs regions; see Fig. 6(b)), forming intensive SF-dislocation interactions. In addition, the SFs multi-directionally form into dense SFs intersections and SFs loops, creating strong SF-SF interactions. The intensive SF-dislocation and SF-SF interactions should result in strain hardening, simultaneously strengthening and elongating the DP-HEA (Nutor et al., 2021). Therefore, the work hardening rate increases with increasing strain, as noted by the first yellow arrow in Fig. 3(c). When the strain reaches 0.1, the work hardening rate increases again with increasing strain. This is supposed to be the generation of MTs. Generally, multi-directional MTs are easily generated in materials with low SFE to coordinate deformation, such as TWIP steel (De Cooman et al., 2018; Li et al., 2022), and consequently result in strong work hardening through twin-twin interactions (Wu et al., 2018). Despite unidirectional, the MTs in the DP-HEA will still refine the FCC matrix to produce dynamic Hall-Petch strengthening (George et al., 2019; Otto et al., 2013), and further together with SFs, hinder the dislocation motion. Hence, twin-dislocation interaction induced hardening enables the work hardening rate to increase again with increasing strain, as noted by the second yellow arrow in Fig. 3(c). Another possible reason for the second yellow arrow is the shear banding effect. Due to severe heterogeneous deformation between the FCC phase and BCC phase, shear banding may be likely formed in this DP-HEA(Frodal et al., 2022; Zhao et al., 2021). Shear banding usually leads to unstable plastic flow (Frint and Wagner, 2019; Sun et al., 2014), inducing the work hardening rate fluctuations. Especially for shear bands at the grain or phase levels, called copper-type shear bands (Duckham et al., 2002, 2001), they usually cause hardening . However, according to the results of Fig. 6, no copper-type shear bands were found in a single phase or in a few contiguous phases. Therefore, SFs and MTs are the main factors that result in the work hardening. On the other hand, the generation of SFs and MTs may the direct reason that the KAM increment at strain from 0.1 to 0.15 is quite large in Fig. 4(c).

Regime III: With further increasing strain, the FCC phase deforms severely and homogeneously. Dislocations are massively nucleated and plane slip occurs within the FCC phase, forming HDD in the form of dense dislocation networks (Fig. 6(a)). In addition to HDD, profuse SFs are continuously developed within the FCC phase, forming numerous SFs intersections and SFs loops (Fig. 6(c)). MTs may also multiply, but their size is still limited to the nanoscale (Fig. 6(d)). On the other hand, only LDD are produced within the BCC phase due to the limited plastic deformation capacity. Therefore, the DP-HEA exhibits significant heterogeneous deformation between the FCC phase and BCC phase.

4.2. Strength contribution of the various factors

As can be seen in Table. 1, The yield strength of the samples corresponding to different laser powers is different. Specifically, as the laser power decreases, the yield strength increases both in tension and compression. Fig. 1 has shown that as the laser power decreases,
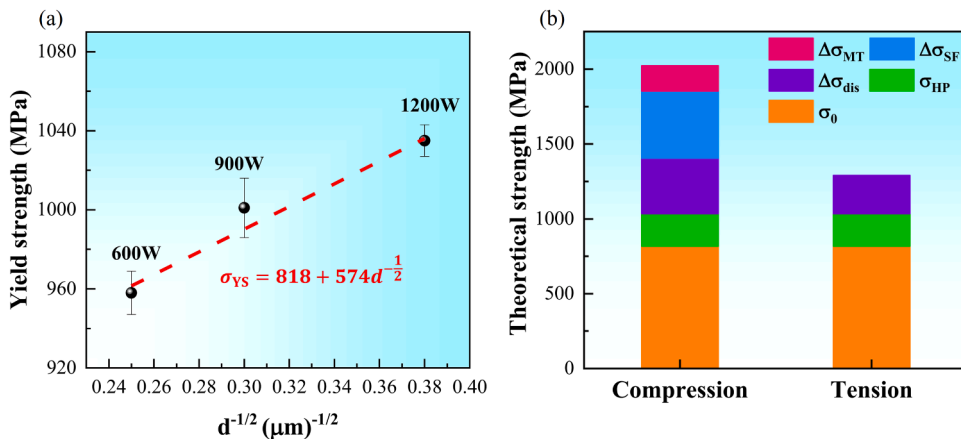

Fig. 7. (a) Hall-Petch relation of the DP-HEA in this work. (b) Contribution of various factors to strength in compression and tension, where σ_{HP} represents the Hall-Petch strengthening.

the grain size gradually decreases while other microstructures do not change significantly. Supposing that the interaction between the phases is attributed to the portion of the intrinsic strength, the difference in yield strength between different samples could be interpreted by the Hall-Petch effect, i.e., the grain refinement strengthening.

The yield strength of the DP-HEA can be expressed as below:

$$\sigma_{YS} = \sigma_0 + \frac{k}{\sqrt{d}}, \tag{3}$$

where σ_0 is the intrinsic strength, k is the Hall-Petch coefficient, d is the grain size. In this work, the σ_0 is calculated as 818 MPa, and k is calculated as 574 MPa•μm$^{-1/2}$, which are determined by plotting the Hall-Petch relation under the three laser power cases in Fig. 7(a).

After deformation, the ultimate strength difference between compression and tension is quite large, which is attributed to the different deformation characteristics inside FCC phase. The compressive ultimate strength can be expressed as below:

$$\sigma_{CUS} = \sigma_0 + \frac{k}{\sqrt{d}} + \Delta\sigma_{dis} + \Delta\sigma_{SF} + \Delta\sigma_{MT} \tag{4}$$

$\Delta\sigma_{dis}$ represents the strength increment contributed by dislocations, which can be further expressed as below:

$$\Delta\sigma_{dis} = M\alpha Gb\sqrt{p}, \tag{5}$$

where M is the Taylor factor, α is a material constant, G is the shear modulus, b is the magnitude of the Burgers vector, and ρ is the dislocation density in the compressive fractured sample. In this work, due to the dislocation density inside the BCC phase being negligible, the dislocation density is only counted inside the FCC phase. Therefore, Eq. (5) needs to be multiplied by a coefficient (ω), as below:

$$\Delta\sigma_{dis} = \omega M\alpha Gb\sqrt{\rho}, \tag{6}$$

where ω is the fraction of the FCC phase. M is taken as 3.06, G is 76.9 GPa, and b is 0.254 nm (Xiong et al., 2020). Considering the calculation difficulty of statically stored dislocation density, the overall dislocation density ρ can be replaced by the GND density, although it may tend to be conservative. According to (Calcagnotto et al., 2010), ρ_{GND} can be quantitatively estimated as below:

$$\rho_{GNDs} = \frac{2\overline{\theta}}{\mu b}, \tag{7}$$

where $\overline{\theta}$ is the average KAM value, μ is the unit length. The ρ_{GND} in the compressive fractured sample is estimated as $\sim 3.4 \times 10^{15}\,m^{-2}$, and therefore, the strength increment contributed by dislocations is $\sim$371 MPa.

$\Delta\sigma_{SF}$ represents the strength increment contributed by SFs (Jian et al., 2013)(Frank et al., 2020), which can be further expressed as below:

$$\Delta\sigma_{SF} = \omega \frac{k_{SF}}{d_{SF}}, \tag{8}$$

where k_{SF} is a strengthening coefficient, d_{SF} is the mean spacing between SFs. In this work, d_{SF} is determined by HRTEM observation ($\sim$5 nm), k_{SF} is 3149 MPa•nm (Frank et al., 2020). Hence, the strength increment contributed by SFs is $\sim$447 MPa.

$\Delta\sigma_{MT}$ represents the strength increment contributed by MTs, i.e., the dynamic Hall-Petch effect. According to Fu et al. (2022)), the $\Delta\sigma_{MT}$ can be expressed as below:

$$\Delta\sigma_{MT} = \omega \frac{2t}{d_{MT} + 2t} \frac{k_{MT}}{\sqrt{t}}, \tag{9}$$

where t is the thickness of the MT, d_{MT} is the spacing between MTs, and k_{MT} is the dynamic Hall-Petch coefficient. In this work, t and d_{MT} are $\sim$3 nm and $\sim$70 nm, determined by TEM observations. k_{MT} is 167 MPa•μm$^{-1/2}$ (Fu et al., 2022). Thus, the strength increment contributed by MTs is $\sim$171 MPa.

The tensile ultimate strength can be only expressed as:

$$\sigma_{TUS} = \sigma_0 + \frac{k}{\sqrt{d}} + \Delta\sigma_{dis}, \tag{10}$$

the ρ_{GND} in the tensile fractured sample is estimated as $\sim 1.6 \times 10^{15}\,m^{-2}$, and therefore, the $\Delta\sigma_{dis}$ is estimated as $\sim$255 MPa.

The strength contribution for each factor in tension and compression are listed in Table 2 and plotted in Fig. 7(b).

4.3. Origin of the TCA in the work hardening

According to the results of EBSD and TEM, the FCC phase behaves more differences between the two deformation paths. In tension, only dislocations are formed within the FCC phase, whereas in compression, in addition to dislocations, numerous SFs and MTs are also

generated within the FCC phase. However, the BCC phase does not behave significantly differently between the two deformation paths, which is only a slight difference in dislocation density. Therefore, the TCA in the work hardening of the DP-HEA is mainly attributed to the SF-dislocation, SF-SF, and twin-dislocation interactions generated within the FCC phase in compression but not in tension. However, why is the deformation behavior of the FCC phase so different between tension and compression? The mystery may be hidden behind the unique alternating lamellar dual-phase heterostructure. The phase boundary (or the BCC phase) plays an important role in the deformation of the FCC phase. Due to the FCC/BCC alternating structure, dislocation in this dual-phase HEA should be nucleated at the phase boundary, since the phase boundary is the weakest (Muskeri et al., 2020) but the energy is the highest here. Dislocations are nucleated massively at the phase boundary and moved towards the FCC phase interior, and eventually blocked by the phase boundary on the other side of the FCC phase, as can be seen in Fig. 8(a) and 8(b). As a result, a large number of dislocations would be piled up at the phase boundary to form DTs, thereby leading to strong localized stress concentration. The strong localized stress concentration may be sufficient to nucleate a crack (Daphalapurkar et al., 2020), of which development in tension and compression may be anisotropic. It is generally considered that the crack surface is open under tension while closed under compression (Wang et al., 2021). In other words, the stress concentration under tension should allow the crack to grow rapidly and in turn, the eventual failure, whereas under compression, the stress concentration should inhibit crack growth, thereby delaying the failure.

To prove the above point, the SEM morphologies are provided in Fig. 9. It can be observed from Fig. 9(a) that extensive voids coalescences and cracks exist inside the tensile fractured sample. Due to the severe stress concentration at the phase boundary, the voids are nucleated and distributed continuously along the phase boundary and start to aggregate, which may be the predecessor of the cracks. With strain increasing, these voids coalescences may develop into a crack parallel to the phase boundary. This type of crack may rapidly propagate since there are no other obstacles along the phase boundary. It can be seen the length and width of the cracks parallel to the phase boundary are ~44.4 μm and ~1.8 μm, respectively. In addition, in the vicinity of the cracks, the FCC and the BCC phases did not undergo obvious morphological changes, indicating that the FCC and the BCC phases have not been sufficiently deformed.

Fig. 9(b) illustrates the SEM morphologies of the compressive sample upon 0.055 strain that corresponds to the strain at tensile fracture of 0.058. Clearly, no visible voids coalescences and cracks are observed at this strain level upon compression. Conversely, some dispersed voids are mainly distributed at grain boundary, in particular boundary triple junction. In addition, small-scale phase breaking is found to form a short crack perpendicular to the phase boundary. These observations prove that the development of defects does respond differently to different deformation paths at the same strain levels. With compressive strain increasing to 0.10 as seen in Fig. 9(c), some phase voids start to coalesce and gradually develop into cracks propagating along grain boundary. Due to the orientation difference between different grains, this type of crack propagates slowly, of which length and width are ~25.6 μm and 0.83 μm, respectively. Meanwhile, the cracks perpendicular to the phase boundary also develop further. However, owing to the interphase interaction, such crack propagation through the phase lamellae is rather difficult, and the length and width of this type of crack are only ~11.1 μm and 0.5 μm, respectively. With further increase in strain until compressive fracture as seen in Fig. 9(d), there are mixed cracks inside the sample, containing the parts that are parallel to the phase boundary and perpendicular to the phase boundary. Compared to the crack only parallel to the phase boundary in the tensile fractured sample, the scale of the mixed crack is relatively small, of which length and width are ~31.3 μm and 1.1 μm, respectively. More importantly, in addition to the mixed crack, shear cracks are formed inside the compressive sample upon this large strain. For shear cracks, the most typical feature is the significant twisting of the phase lamellae adjacent to this type of crack. This is strongly different from the cracks in the tensile fractured sample. Also, some micro-level shear bands limited to a lamellar colony are formed, which are evidence of shear events and the resultant shear cracks. The length and width of the shear crack are ~26.2 μm and 1.0 μm, respectively. Likewise, it is also much smaller than the scale of the cracks in the tensile fractured sample.

According to the results of Fig. 9, the hidden origin of tension-compression asymmetry in the work hardening may be revealed. This asymmetry is mainly attributed to the strongly different crack development between tension and compression. In tension, single type of crack parallel to the phase boundary propagate rapidly and cause premature failure of the sample. In compression, various types of cracks (such as cracks perpendicular to the phase boundary, cracks along to grain boundary and shear cracks) are produced. These cracks develop slowly due to different obstacles, which delays the failure of the sample. Therefore, in compression, the sample will continue to deform, reaching the critical resolved shear stress for SFs and MTs at the phase boundary, as can be seen in Figs. 8(c) and 8 (d).

4.4. Effect of heterogeneous deformation on the TCA in work hardening

Fig. 3(c) demonstrates that the magnitude of the TCA in the work hardening of the DP-HEA is lower than that of the single-phase $Al_{0.3}CoCrFeNi$ HEA. This may be due to the relative scale and content of the MTs in this DP-HEA. The lamellar heterostructure divides the FCC phase into countless islands that cannot be connected, and phase boundary are uniformly distributed inside the DP-HEA. Even if the MTs are initiated within the FCC phase, their development will be limited due to the small size of the independent islands. Also, the presence of the phase boundary may inhibit the propagation and connection of the MTs. For instance, the size of the MTs in the DP-

Table 2
Contribution of the various factors to the ultimate strength.

	σ_0 (MPa)	σ_{HP} (MPa)	$\Delta\sigma_{dis}$ (MPa)	$\Delta\sigma_{SF}$ (MPa)	$\Delta\sigma_{MT}$ (MPa)
Compression	818	217	371	447	171
Tension	818	217	255	\	\

Strain to 0.05

Strain to 0.1
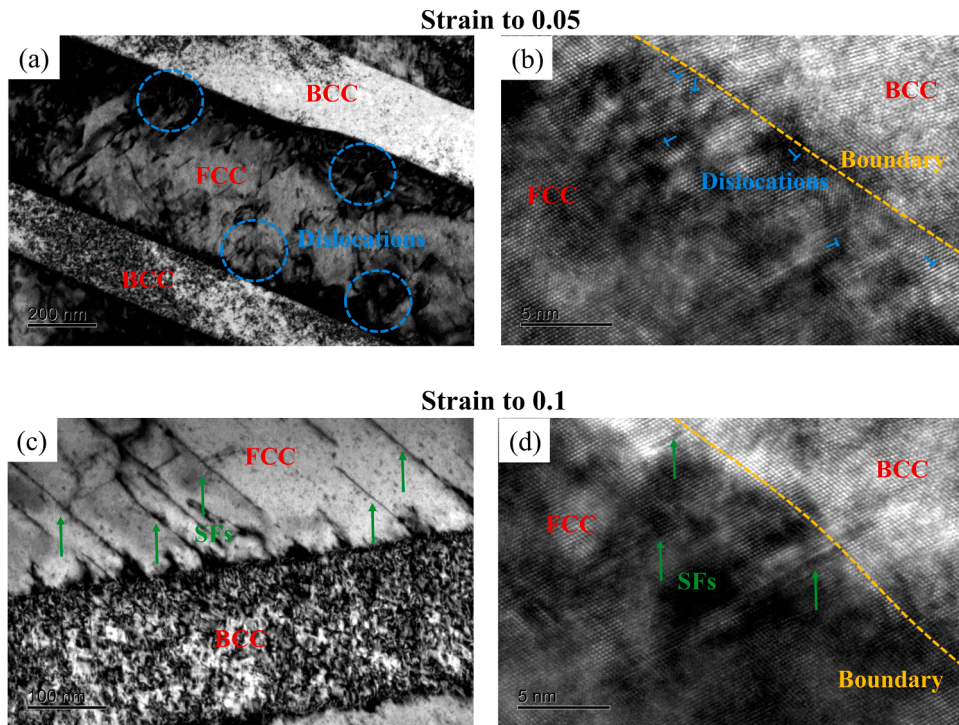
Fig. 8. (a) and (b) dislocations nucleated at the phase boundary. (c) and (d) SFs nucleated at the phase boundary.

HEA is quite small (less than 5 nm), which is far less than that in the $Al_{0.3}CoCrFeNi$ HEA (~50 μm). In addition to the MTs scale, the conditions for the advent of MTs are also different between the DP-HEA and the $Al_{0.3}CoCrFeNi$ HEA. When the strain reaches 0.35, the latter begins to show MTs. However, according to the work hardening rate curve (Fig. 3(c)), when the strain reaches 0.1, MTs have already occurred in the DP-HEA. The earlier formation of MTs in the DP-HEA may be attributed to the accumulation of dislocations within the FCC phase. Compared with the $Al_{0.3}CoCrFeNi$ HEA, the FCC phase in the DP-HEA may experience larger stress amplitudes earlier, thus reaching the critical resolved shear stress for twinning initiation. While the MTs may be generated earlier with the FCC phase of the DP-HEA, MTs are more difficult in developing due to the small FCC island as well as the inhibition of the BCC phase.

4.5. Alterable TCA in the work hardening of the DP-HEA

As discussed above, the DP-HEA shows a reduced TCA in work hardening due to the heterogeneous deformation. More interestingly, the TCA in the work hardening of the DP-HEA is alterable. As Fig. 3(b) shows, D_2 values of the DP-HEA printed at 1200 W, 900 W, and 600 W are ~36, ~50, and ~22, respectively. Since the three samples have different microstructures such as phase fraction and phase width (Figs. 1 and 2), this means that microstructural characteristics directly determine the degree of the TCA in work hardening. To further confirm the viewpoint, KAM profiles of the FCC phase and the BCC phase after compression are provided in Fig. 10.

The average KAM values of the FCC phase of the DP-HEA printed at 1200 W, 900 W, and 600 W are 0.71±0.18°, 0.82±0.21°, and 0.67±0.23°, respectively. It can be seen from Fig. 10(a) that the increasing trend of the KAM value is the same as that of the D_2. Whereas, the average KAM values of the BCC phase of the DP-HEA printed at 1200 W, 900 W, and 600 W are 0.47±0.19°, 0.48±0.14°, and 0.46±0.15°, respectively. These values are hardly any changed. It can be seen from Fig. 10(b) that the three profiles are almost overlap, indicating the deformation of the BCC phase of different samples is at the same level in compression. Therefore, it can be speculated that only the degree of deformation of the FCC phase determines the magnitude of the D_2.

It can be inferred that the KAM value of the FCC phase of the DP-HEA printed at 600 W is the smallest due to relatively low SFs and MTs contents. First, the DP-HEA printed at 600 W has the lowest FCC fraction (Fig. 2(b)), which inevitably leads to fewer SFs and MTs. Another possible reason is that the FCC phase width of the DP-HEA printed at 600 W is the smallest (Fig. 2(a)). MTs are very sensitive to grain size, that is, the smaller the grain size, the larger the critical resolved shear stress for twinning. These two key factors may together contribute to the decrease in D_2, which is reflected in the decrease in KAM value. On the other hand, the phase width ratio of the FCC phase to the BCC phase (referred to as the phase width ratio) has a significant effect not only on the compressive deformation but also on the tensile deformation. It can be observed that the phase width ratio of the DP-HEA printed at 600 W is the smallest at 1.96, indicating that the alternating lamellae of the FCC phase and BCC phase are more compact, and there are more phase boundaries evenly distributed. In this case, two results may be raised. In compression, the development of the SFs and MTs may be suppressed due to densely arranged grain boundaries, which weakens the interactions between the multiple defects comprising dislocations, SFs, and MTs. Therefore, the work hardening during compression will be significantly inhibited. In tension, localized stress concentration at a
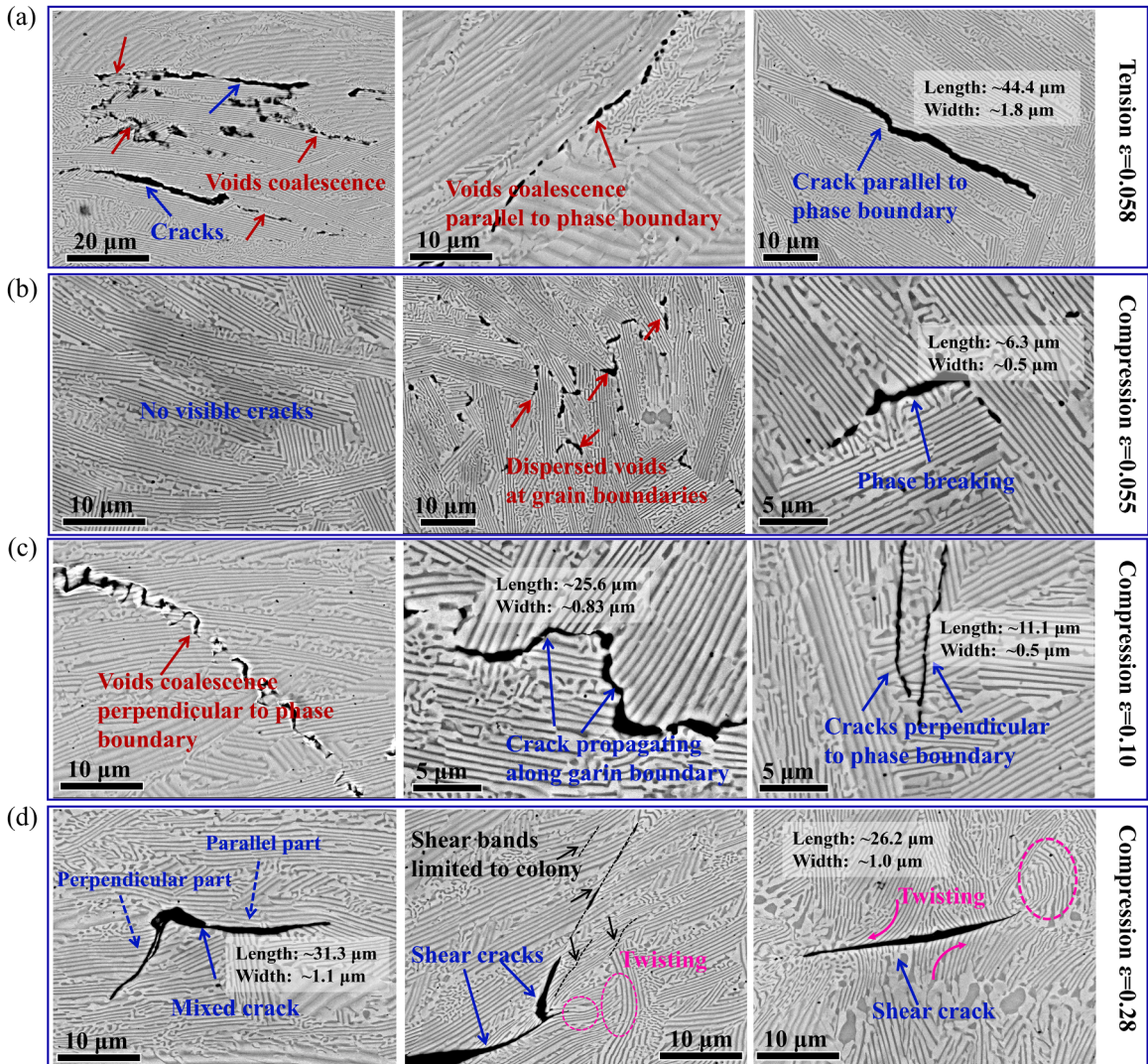
Fig. 9. The SEM morphologies of (a) the tensile sample after fracture, and the compressive one at strain magnitude of (b) 0.055, (c) 0.10 and (d) 0.28 (fracture), respectively. Tensile sample presents most cracks parallel to the phase boundary, which indicates debonding at phase interface as the failure mechanism. However, the compressive sample exhibit a large variety in the form of cracks, postponing failure compared with case of tension. All the SEM sectioning is done parallel to the loading axis.

single phase boundary will be significantly reduced due to the increase in the overall boundary density, improving the overall uniform plastic deformation.

Conclusion

To acquire an in-depth understanding of the origin of TCA in the work hardening of the multi-domain HEAs, an AlCoCrFeNi$_{2.1}$ dual-phase HEA with three distinct microstructures was prepared by additive manufacturing. The mechanical performance was tested both in compression and tension, and the microstructures before and after deformation were characterized and analyzed by SEM, EBSD and TEM/HRTEM. The main conclusions are as follows:

(1) The DP-HEA exhibits a negligible TCA in the yielding but a conspicuous TCA in the work hardening. This is primarily attributed to the interactions between multiple defects (containing dislocations, SFs, and MTs) generated within the FCC phase in compression but not in tension. The SF-dislocation interaction and SF-SF interaction are dominant, which not only provides strong strengthening as barriers for dislocation movement but also enables considerable plasticity. MTs are generated in dense SFs regions to accommodate plastic deformation, which then forms twin-dislocation interactions that bring additional strain hardening.
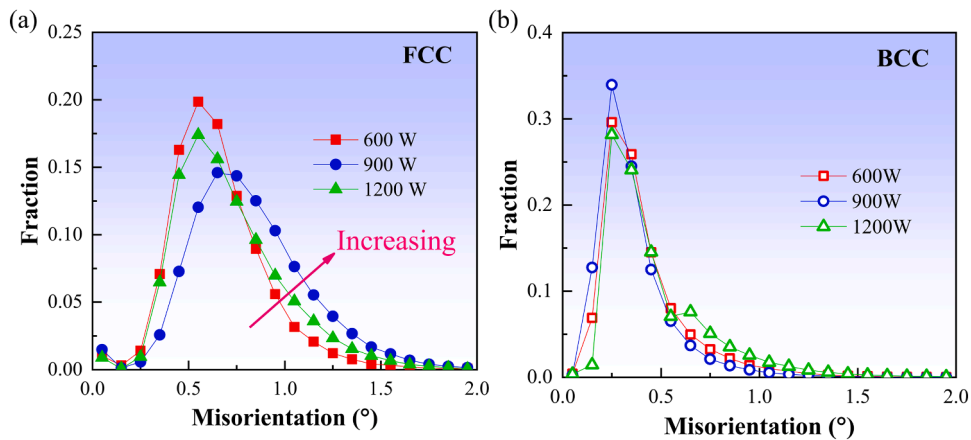
Fig. 10. KAM profiles of (a) the FCC phase and (b) the BCC phase of the various DP-HEA after compression, indicating that the deformation of the FCC phase has a decisive effect on the D_2.

(2) The unique alternating lamellar structure of the DP-HEA will lead to intensive localized stress concentration at the phase boundary due to heterogeneous deformation. In tension, the stress concentration can cause cracks parallel to the phase boundary, which rapidly develops and results in the DP-HEA premature fracture, whereas in compression, various types of cracks are formed and develop slowly, the failure of the DP-HEA could be postponed, providing the opportunity for the nucleation of SFs and MTs.

(3) The degree of the TCA in this DP-HEA is less than in the single-phase HEA. In addition, this TCA in the DP-HEA seems alterable. By tailoring the geometry of the alternating lamellar structure, the level of the TCA in the work hardening can be reduced to some extent. In the future, by designing hierarchical heterostructures (such as bi-modal grains structure, gradient structure, dual- or multi-phase structure and harmonic structure) to achieve the tunable possibility of the TCA in the work hardening may become a promising strategy.

CRediT authorship contribution statement

Yunjian Bai: Conceptualization, Methodology, Investigation, Writing – original draft, Writing – review & editing. **Kun Zhang:** Conceptualization, Methodology, Validation, Supervision, Resources, Project administration, Writing – review & editing. **Tianyu Chen:** Writing – review & editing. **Zishang Liu:** Methodology, Writing – review & editing. **Yunjiang Wang:** Methodology, Writing – review & editing. **Bingchen Wei:** Conceptualization, Methodology, Validation, Supervision, Funding acquisition, Resources, Project administration, Writing – review & editing.

Declaration of Competing Interest

The authors declare that they have no known competing financial interests or personal relationships that could have appeared to influence the work reported in this paper.

Data availability

Data will be made available on request.

Acknowledgments

Supplementary materials

Supplementary material associated with this article can be found, in the online version, at doi:10.1016/j.ijplas.2022.103432.

References

An, X., Wang, Z., Ni, S., Song, M., 2020. The tension-compression asymmetry of martensite phase transformation in a metastable Fe40Co20Cr20Mn10Ni10 high-entropy alloy. Sci. China Mater. 63, 1797–1807. https://doi.org/10.1007/s40843-020-1319-3.

Bai, Y., Jiang, H., Yan, K., Li, M., Wei, Y., Zhang, K., Wei, B., 2021. Phase transition and heterogeneous strengthening mechanism in CoCrFeNiMn high-entropy alloy fabricated by laser-engineered net shaping via annealing at intermediate-temperature. J. Mater. Sci. Technol. 92, 129–137. https://doi.org/10.1016/j.jmst.2021.03.028.

Calcagnotto, M., Ponge, D., Demir, E., Raabe, D., 2010. Orientation gradients and geometrically necessary dislocations in ultrafine grained dual-phase steels studied by 2D and 3D EBSD. Mater. Sci. Eng. A 527, 2738–2746. https://doi.org/10.1016/j.msea.2010.01.004.

Cao, Z.H., Zhai, G.Y., Ma, Y.J., Ding, L.P., Li, P.F., Liu, H.L., Lu, H.M., Cai, Y.P., Wang, G.J., Meng, X.K., 2021. Evolution of interfacial character and its influence on strain hardening in dual-phase high entropy alloys at nanoscale. Int. J. Plast. 145 https://doi.org/10.1016/j.ijplas.2021.103081.

Cepeda-Jiménez, C.M., Castillo-Rodríguez, M., Pérez-Prado, M.T., 2019. Origin of the low precipitation hardening in magnesium alloys. Acta Mater. 165, 164–176. https://doi.org/10.1016/j.actamat.2018.11.044.

Chen, C., Huang, H., Niu, J., Nie, J.F., Yuan, G., 2021. Origin of high tension-compression yield asymmetry in as-extruded pure zinc. Scr. Mater. 200, 113922 https://doi.org/10.1016/j.scriptamat.2021.113922.

Daphalapurkar, N.P., Luscher, D.J., Versino, D., Margolin, L., Hunter, A., 2020. An anisotropic damage model based on dislocation-mediated nucleation of cracks under high-rate compression. J. Mech. Phys. Solids 137. https://doi.org/10.1016/j.jmps.2019.103818.

De Cooman, B.C., Estrin, Y., Kim, S.K., 2018. Twinning-induced plasticity (TWIP) steels. Acta Mater. 142, 283–362. https://doi.org/10.1016/j.actamat.2017.06.046.

Deng, Y., Tasan, C.C., Pradeep, K.G., Springer, H., Kostka, A., Raabe, D., 2015. Design of a twinning-induced plasticity high entropy alloy. Acta Mater. 94, 124–133. https://doi.org/10.1016/j.actamat.2015.04.014.

Duckham, A., Engler, O., Knutsen, R.D., 2002. Moderation of the recrystallization texture by nucleation at copper-type shear bands in Al-1Mg. Acta Mater. 50, 2881–2893. https://doi.org/10.1016/S1359-6454(02)00112-X.

Duckham, A., Knutsen, R.D., Engler, O., 2001. Influence of deformation variables on the formation of copper-type shear bands in Al-1Mg. Acta Mater. 49, 2739–2749. https://doi.org/10.1016/S1359-6454(01)00166-5.

Fang, Q., Chen, Y., Li, J., Jiang, C., Liu, B., Liu, Y., Liaw, P.K., 2019. Probing the phase transformation and dislocation evolution in dual-phase high-entropy alloys. Int. J. Plast. 114, 161–173. https://doi.org/10.1016/j.ijplas.2018.10.014.

Frank, M., Nene, S.S., Chen, Y., Gwalani, B., Kautz, E.J., Devaraj, A., An, K., Mishra, R.S., 2020. Correlating work hardening with co-activation of stacking fault strengthening and transformation in a high entropy alloy using in-situ neutron diffraction. Sci. Rep. 10, 1–10. https://doi.org/10.1038/s41598-020-79492-8.

Frint, P., Wagner, M.F.X., 2019. Strain partitioning by recurrent shear localization during equal-channel angular pressing of an AA6060 aluminum alloy. Acta Mater. 176, 306–317. https://doi.org/10.1016/j.actamat.2019.07.009.

Frodal, B.H., Thomesen, S., Børvik, T., Hopperstad, O.S., 2022. On fracture anisotropy in textured aluminium alloys. Int. J. Solids Struct. 111563, 244–245. https://doi.org/10.1016/j.ijsolstr.2022.111563.

Fu, W., Huang, Y., Sun, J., Ngan, A.H.W., 2022. Strengthening CrFeCoNiMn0.75Cu0.25 high entropy alloy via laser shock peening. Int. J. Plast. 154, 103296 https://doi.org/10.1016/j.ijplas.2022.103296.

Gao, X., Lu, Y., Zhang, B., Liang, N., Wu, G., Sha, G., Liu, J., Zhao, Y., 2017. Microstructural origins of high strength and high ductility in an AlCoCrFeNi2.1 eutectic high-entropy alloy. Acta Mater. 141, 59–66. https://doi.org/10.1016/j.actamat.2017.07.041.

George, E.P., Raabe, D., Ritchie, R.O., 2019. High-entropy alloys. Nat. Rev. Mater. https://doi.org/10.1038/s41578-019-0121-4.

Ghorbanpour, S., Alam, M.E., Ferreri, N.C., Kumar, A., McWilliams, B.A., Vogel, S.C., Bicknell, J., Beyerlein, I.J., Knezevic, M., 2020. Experimental characterization and crystal plasticity modeling of anisotropy, tension-compression asymmetry, and texture evolution of additively manufactured Inconel 718 at room and elevated temperatures. Int. J. Plast. 125, 63–79. https://doi.org/10.1016/j.ijplas.2019.09.002.

Gludovatz, B., Hohenwarter, A., Catoor, D., Chang, E.H., George, E.P., Ritchie, R.O., 2014. A fracture-resistant high-entropy alloy for cryogenic applications. Science 345 (80–), 1153–1158. https://doi.org/10.1126/science.1254581.

Gorsse, S., Miracle, D.B., Senkov, O.N., 2017. Mapping the world of complex concentrated alloys. Acta Mater. 135, 177–187. https://doi.org/10.1016/j.actamat.2017.06.027.

Habib, S.A., Khan, A.S., Gnäupel-Herold, T., Lloyd, J.T., Schoenfeld, S.E., 2017. Anisotropy, tension-compression asymmetry and texture evolution of a rare-earth-containing magnesium alloy sheet, ZEK100, at different strain rates and temperatures: experiments and modeling. Int. J. Plast. 95, 163–190. https://doi.org/10.1016/j.ijplas.2017.04.006.

Hasan, M.N., Liu, Y.F., An, X.H., Gu, J., Song, M., Cao, Y., Li, Y.S., Zhu, Y.T., Liao, X.Z., 2019. Simultaneously enhancing strength and ductility of a high-entropy alloy via gradient hierarchical microstructures. Int. J. Plast. 123, 178–195. https://doi.org/10.1016/j.ijplas.2019.07.017.

He, F., Yang, Z., Liu, S., Chen, D., Lin, W., Yang, T., Wei, D., Wang, Z., Wang, J., Kai, J.jung, 2021a. Strain partitioning enables excellent tensile ductility in precipitated heterogeneous high-entropy alloys with gigapascal yield strength. Int. J. Plast. 144, 103022 https://doi.org/10.1016/j.ijplas.2021.103022.

He, Z., Jia, N., Yan, H., Shen, Y., Zhu, M., Guan, X., Zhao, X., Jin, S., Sha, G., Zhu, Y., Liu, C.T., 2021b. Multi-heterostructure and mechanical properties of N-doped FeMnCoCr high entropy alloy. Int. J. Plast. 139, 102965 https://doi.org/10.1016/j.ijplas.2021.102965.

Jeong, J., Alfreider, M., Konetschnik, R., Kiener, D., Oh, S.H., 2018. In-situ TEM observation of {101‾2} twin-dominated deformation of Mg pillars: twinning mechanism, size effects and rate dependency. Acta Mater. 158, 407–421. https://doi.org/10.1016/j.actamat.2018.07.027.

Jian, W.W., Cheng, G.M., Xu, W.Z., Koch, C.C., Wang, Q.D., Zhu, Y.T., Mathaudhu, S.N., 2013. Physics and model of strengthening by parallel stacking faults. Appl. Phys. Lett. 103 https://doi.org/10.1063/1.4822323.

Jiang, R., Bull, D.J., Evangelou, A., Harte, A., Pierron, F., Sinclair, I., Preuss, M., Hu, X.T., Reed, P.A.S., 2018. Strain accumulation and fatigue crack initiation at pores and carbides in a SX superalloy at room temperature. Int. J. Fatigue 114, 22–33. https://doi.org/10.1016/j.ijfatigue.2018.05.003.

Joseph, J., Stanford, N., Hodgson, P., Fabijanic, D.M., 2017. Tension/compression asymmetry in additive manufactured face centered cubic high entropy alloy. Scr. Mater. 129, 30–34. https://doi.org/10.1016/j.scriptamat.2016.10.023.

Khan, A.S., Liu, H., 2012. Strain rate and temperature dependent fracture criteria for isotropic and anisotropic metals. Int. J. Plast. 37, 1–15. https://doi.org/10.1016/j.ijplas.2012.01.012.

Khan, A.S., Yu, S., 2012. Deformation induced anisotropic responses of Ti-6Al-4V alloy. Part I: experiments. Int. J. Plast. 38, 14–26. https://doi.org/10.1016/j.ijplas.2012.03.015.

Khan, A.S., Yu, S., Liu, H., 2012. Deformation induced anisotropic responses of Ti-6Al-4V alloy Part II: a strain rate and temperature dependent anisotropic yield criterion. Int. J. Plast. 38, 14–26. https://doi.org/10.1016/j.ijplas.2012.03.013.

Ku, A.Y., Khan, A.S., Gnäupel-Herold, T., 2020. Quasi-static and dynamic response, and texture evolution of two overaged Al 7056 alloy plates in T761 and T721 tempers: experiments and modeling. Int. J. Plast. 130 https://doi.org/10.1016/j.ijplas.2020.102679.

Li, J., Chen, H., Fang, Q., Jiang, C., Liu, Y., Liaw, P.K., 2020a. Unraveling the dislocation-precipitate interactions in high-entropy alloys. Int. J. Plast. 133, 102819 https://doi.org/10.1016/j.ijplas.2020.102819.

Li, Q., Xue, S., Zhang, Y., Sun, X., Wang, H., Zhang, X., 2020b. Plastic anisotropy and tension-compression asymmetry in nanotwinned Al-Fe alloys: an in-situ micromechanical investigation. Int. J. Plast. 132, 102760 https://doi.org/10.1016/j.ijplas.2020.102760.

Li, Y.Z., Liang, Z.Y., Huang, M.X., 2022. Strengthening contributions of dislocations and twins in warm-rolled TWIP steels. Int. J. Plast. 150 https://doi.org/10.1016/j.ijplas.2021.103198.

Lin, P., Hao, Y., Zhang, B., Zhang, S., Chi, C., Shen, J., 2017. Tension-compression asymmetry in yielding and strain hardening behavior of CP-Ti at room temperature. Mater. Sci. Eng. A 707, 172–180. https://doi.org/10.1016/j.msea.2017.09.042.

Liu, L., Zhang, Y., Li, J., Fan, M., Wang, X., Wu, G., Yang, Z., Luan, J., Jiao, Z., Liu, C.T., Liaw, P.K., Zhang, Z., 2022. Enhanced strength-ductility synergy via novel bifunctional nano-precipitates in a high-entropy alloy. Int. J. Plast. 153, 103235 https://doi.org/10.1016/j.ijplas.2022.103235.

Ma, E., Wu, X., 2019. Tailoring heterogeneities in high-entropy alloys to promote strength–ductility synergy. Nat. Commun. 10, 1–10. https://doi.org/10.1038/s41467-019-13311-1.

Miracle, D.B., Senkov, O.N., 2017. A critical review of high entropy alloys and related concepts. Acta Mater. 122, 448–511. https://doi.org/10.1016/j.actamat.2016.08.081.

Muskeri, S., Hasannaeimi, V., Salloom, R., Sadeghilaridjani, M., Mukherjee, S., 2020. Small-scale mechanical behavior of a eutectic high entropy alloy. Sci. Rep. 10, 1–12. https://doi.org/10.1038/s41598-020-59513-2.

Nutor, R.K., Cao, Q., Wei, R., Su, Q., Du, G., Wang, X., Li, F., Zhang, D., Jiang, J.Z., 2021. A dual-phase alloy with ultrahigh strength-ductility synergy over a wide temperature range. Sci. Adv. 7, 1–8. https://doi.org/10.1126/sciadv.abi4404.

Otto, F., Dlouhý, A., Somsen, C., Bei, H., Eggeler, G., George, E.P., 2013. The influences of temperature and microstructure on the tensile properties of a CoCrFeMnNi high-entropy alloy. Acta Mater. 61, 5743–5755. https://doi.org/10.1016/j.actamat.2013.06.018.

Park, S.H., Lee, J.H., Moon, B.G., You, B.S., 2014. Tension-compression yield asymmetry in as-cast magnesium alloy. J. Alloy. Compd. 617, 277–280. https://doi.org/10.1016/j.jallcom.2014.07.164.

Qin, S., Yang, M., Jiang, P., Wang, J., Wu, X., Zhou, H., Yuan, F., 2022. Designing structures with combined gradients of grain size and precipitation in high entropy alloys for simultaneous improvement of strength and ductility. Acta Mater. 230, 117847 https://doi.org/10.1016/j.actamat.2022.117847.

Sathiyamoorthi, P., Kim, H.S., 2022. High-entropy alloys with heterogeneous microstructure: processing and mechanical properties. Prog. Mater. Sci. 123, 100709 https://doi.org/10.1016/j.pmatsci.2020.100709.

Sun, J., Yang, Z., Liu, H., Han, J., Wu, Y., Zhuo, X., Song, D., Jiang, J., Ma, A., Wu, G., 2019. Tension-compression asymmetry of the AZ91 magnesium alloy with multi-heterogenous microstructure. Mater. Sci. Eng. A 759, 703–707. https://doi.org/10.1016/j.msea.2019.05.093.

Sun, J.L., Trimby, P.W., Yan, F.K., Liao, X.Z., Tao, N.R., Wang, J.T., 2014. Shear banding in commercial pure titanium deformed by dynamic compression. Acta Mater. 79, 47–58. https://doi.org/10.1016/j.actamat.2014.07.011.

Suryawanshi, J., Singh, G., Msolli, S., Jhon, M.H., Ramamurty, U., 2021. Tension-compression asymmetry and shear strength of titanium alloys. Acta Mater. 221, 117392 https://doi.org/10.1016/j.actamat.2021.117392.

Wang, Y., Ding, J., Fan, Z., Tian, L., Li, M., Lu, H., Zhang, Y., Ma, E., Li, J., Shan, Z., 2021. Tension–compression asymmetry in amorphous silicon. Nat. Mater. 20, 1371–1377. https://doi.org/10.1038/s41563-021-01017-z.

Wang, Z., Wang, C., Zhao, Y.L., Hsu, Y.C., Li, C.L., Kai, J.J., Liu, C.T., Hsueh, C.H., 2020. High hardness and fatigue resistance of CoCrFeMnNi high entropy alloy films with ultrahigh-density nanotwins. Int. J. Plast. 131, 102726 https://doi.org/10.1016/j.ijplas.2020.102726.

Wu, S.W., Wang, G., Jia, Y.D., Yi, J., Zhai, Q.J., Liu, C.T., Sun, B.A., Chu, H.J., Shen, J., Liaw, P.K., Zhang, T.Y., 2019. Enhancement of strength-ductility trade-off in a high-entropy alloy through a heterogeneous structure. Acta Mater. 165, 444–458. https://doi.org/10.1016/j.actamat.2018.12.012.

Wu, Y., Bönisch, M., Alkan, S., Abuzaid, W., Sehitoglu, H., 2018. Experimental determination of latent hardening coefficients in FeMnNiCoCr. Int. J. Plast. 105, 239–260. https://doi.org/10.1016/j.ijplas.2018.02.016.

Xiong, T., Zheng, S., Pang, J., Ma, X., 2020. High-strength and high-ductility AlCoCrFeNi2.1 eutectic high-entropy alloy achieved via precipitation strengthening in a heterogeneous structure. Scr. Mater. 186, 336–340. https://doi.org/10.1016/j.scriptamat.2020.04.035.

Xu, X.D., Liu, P., Tang, Z., Hirata, A., Song, S.X., Nieh, T.G., Liaw, P.K., Liu, C.T., Chen, M.W., 2018. Transmission electron microscopy characterization of dislocation structure in a face-centered cubic high-entropy alloy Al0.1CoCrFeNi. Acta Mater. 144, 107–115. https://doi.org/10.1016/j.actamat.2017.10.050.

Ye, Y.F., Wang, Q., Lu, J., Liu, C.T., Yang, Y., 2016. High-entropy alloy: challenges and prospects. Mater. Today. https://doi.org/10.1016/j.mattod.2015.11.026.

Yin, D.D., Boehlert, C.J., Long, L.J., Huang, G.H., Zhou, H., Zheng, J., Wang, Q.D., 2021. Tension-compression asymmetry and the underlying slip/twinning activity in extruded Mg-Y sheets. Int. J. Plast. 136, 102878 https://doi.org/10.1016/j.ijplas.2020.102878.

Zhang, J.Y., He, Q.F., Li, J., Yang, Y., 2021. Chemical fluctuation enabling strength-plasticity synergy in metastable single-phase high entropy alloy film with gigapascal yield strength. Int. J. Plast. 139 https://doi.org/10.1016/j.ijplas.2021.102951.

Zhao, H.Z., You, Z.S., Tao, N.R., Lu, L., 2021. Anisotropic strengthening of nanotwin bundles in heterogeneous nanostructured Cu: effect of deformation compatibility. Acta Mater. 210 https://doi.org/10.1016/j.actamat.2021.116830.